



LAWRENCE
LIVERMORE
NATIONAL
LABORATORY

An explicitly coupled hydro-geomechanical model for simulating hydraulic fracturing in complex discrete fracture networks

P. Fu, S. M. Johnson, C. R. Carrigan

December 7, 2011

International Journal for Numerical and Analytical Methods in
Geomechanics

Disclaimer

This document was prepared as an account of work sponsored by an agency of the United States government. Neither the United States government nor Lawrence Livermore National Security, LLC, nor any of their employees makes any warranty, expressed or implied, or assumes any legal liability or responsibility for the accuracy, completeness, or usefulness of any information, apparatus, product, or process disclosed, or represents that its use would not infringe privately owned rights. Reference herein to any specific commercial product, process, or service by trade name, trademark, manufacturer, or otherwise does not necessarily constitute or imply its endorsement, recommendation, or favoring by the United States government or Lawrence Livermore National Security, LLC. The views and opinions of authors expressed herein do not necessarily state or reflect those of the United States government or Lawrence Livermore National Security, LLC, and shall not be used for advertising or product endorsement purposes.

An explicitly coupled hydro-geomechanical model for simulating hydraulic fracturing in complex discrete fracture networks

Pengcheng Fu*, Scott M. Johnson, and Charles R. Carrigan

Atmospheric, Earth, and Energy Division, Lawrence Livermore National Laboratory

* Corresponding author; fu4@llnl.gov; 1-925-422-3579

Abstract:

Modeling hydraulic fracturing in the presence of a natural fracture network is a challenging task, owing to the complex interactions between fluid, rock matrix, and rock interfaces, as well as the interactions between propagating fractures and existing natural interfaces. Understanding these complex interactions through numerical modeling is critical to the design of optimum stimulation strategies. In this paper, we present an explicitly integrated, fully coupled discrete-finite element approach for the simulation of hydraulic fracturing in complex fracture networks. The individual physical processes involved in hydraulic fracturing are identified and addressed as separate modules: a finite element approach for geomechanics in the rock matrix, a finite volume approach for resolving hydrodynamics, a geomechanical joint model for interfacial resolution, and an adaptive remeshing module. The model is verified against the KGD closed-form solution for the propagation of a single hydraulic fracture and validated against laboratory testing results on the interaction between a propagating hydraulic fracture and an existing fracture. Preliminary results of simulating hydraulic fracturing in a relatively complex natural fracture system are also presented.

Keywords: Hydraulic fracture; discrete fracture network; explicit coupling; fracture interaction; rock joint; reservoir model

1. INTRODUCTION

Hydraulic fracturing is widely used by the energy industry (e.g., stimulation of gas shales, enhanced geothermal systems, etc.) to increase permeability of geological formations through the creation of hydraulically driven fractures and coupling of these new higher permeability flow paths with the natural fracture networks in the rock. A number of methods have been developed to make direct and indirect field observations on the hydraulic fracturing process, including mineback experiments, tiltmeter and microseismic mapping, pumping pressure diagnosis, etc. [1-4]. Numerous analytical and numerical hydraulic fracturing models have been developed to explain these observations (e.g. [5-10]). Despite the variety of existing models, there remains a gap between the state-of-the-art methodologies for modeling hydraulic fractures and the imminent needs of industry to improve prediction of hydraulically-driven fracture behavior in the presence of complex preexisting fracture networks at field scales. Field data have demonstrated the complex patterns of new hydraulic fractures and re-mobilized preexisting fractures in naturally fractured reservoirs (e.g. [1, 11]). However, much attention from the hydraulic fracture modeling community has focused on scenarios with highly idealized fracture geometries. The classic PKN and KGD models [5, 7-9] and contemporary incarnations (e.g. [12, 13]) only address propagation of

a single fracture with assumed geometries in a homogeneous medium. The pseudo-3D (P3D) and planar 3D (PL3D) models [10, 14] are capable of addressing some of the issues with the homogeneous medium assumption by simulating fractures vertically extending through multiple geologic layers, but each simulation can only handle one crack lying in a single vertical plane. Other available numerical models for hydraulic fracturing generally approach modeling from one of two directions: rigorously address the solid-fluid coupling for a single fracture in a homogenous medium or address the relatively complex network but with little or no ability to capture the creation of new fractures [15-20].

Here we present a numerical method for simulating hydraulically-driven fracturing in relatively complex preexisting/natural fracture systems, under the assumptions of quasi-static plane-strain deformation, laminar Newtonian flow, and an impermeable rock matrix. This numerical model is akin to a numerical extension of the KGD model with the additional ability to handle arbitrary rock toughness and the interactions between multiple fractures. The organization of the paper is as follows: Section 2 of the paper describes the overall simulation strategy and the coupling scheme between the multiple physical processes involved. The algorithmic aspects of the individual components in the model are described in Section 3. In Sections 4 and 5, we verify and validate the model against available closed-form solutions for the propagation of a single fracture and laboratory experimental data on the interaction between two fractures, respectively. Finally, we present preliminary results on using the numerical model to simulate the stimulation of a naturally fractured reservoir with a complex preexisting fracture network.

2. STIMULATION STRATEGY AND COUPLING SCHEME

The aforementioned gap between existing simulation capabilities and need for modeling complex fracture systems is largely due to the intrinsically complex nature of the hydraulic fracturing process. A variety of inter-dependent physical mechanisms, including flow within the discrete fracture network in the presence of changing joint permeability, rock deformation due to both interaction between the pressurized fluid in the joint and changing stresses within the rock matrix, and evolution of the fracture network and rock matrix topology as fractures propagate over time, must be appropriately handled to result in reasonable hydraulic fracturing simulation.

Existing analytical models often accommodate the interactions between the above mechanisms by implicitly coupling them into the governing equations. Because of the complexity of the interactions, only a subset of the mechanisms, usually in highly simplified and idealized forms can be incorporated into such equations. To avoid this limitation, our numerical model adopts an explicit coupling simulation strategy where individual modules are developed to model these distinct physical mechanisms with their interactions embodied by the data/information exchange between the modules. Because the solid and fluid solvers share the same time-integration approaches, the overall error from this approach coupling remains second-order. Important modules in our numerical model include:

- A finite element method (FEM) geomechanics solver with linearly elastic elements and a linear elastic fracture mechanics (LEFM) component to resolve trajectory and growth rate of propagating fractures.

- A finite volume method (FVM) hydrodynamics flow solver for viscous, laminar flow.
- A geomechanical joint model to capture the nonlinear, hysteretic behavior of the interfacial interactions as well as the coupling to permeability changes.
- An adaptive remeshing module for generating topologically compatible meshes between the finite elements and finite volume elements.

Figure 1 illustrates the coupling of these modules. The algorithmic aspects are described in the next section. In real geological settings a number of additional phenomena may be important depending on the application, including anisotropy, creep, geochemical interactions, thermal effects, etc., which are beyond the scope of this approach. The objective here is to develop a numerical model compatible with the KGD model but with the additional capabilities of handling interactions between fractures and a more rigorous treatment of fracture mechanics than that model affords. The formulations of the constitutive modules in this paper serve this objective and thus simple forms are preferred. Because of the modular design of the simulation framework and the explicit coupling method, each module can be easily modified or upgraded when necessary, as long as the interfaces with other modules are appropriately handled.

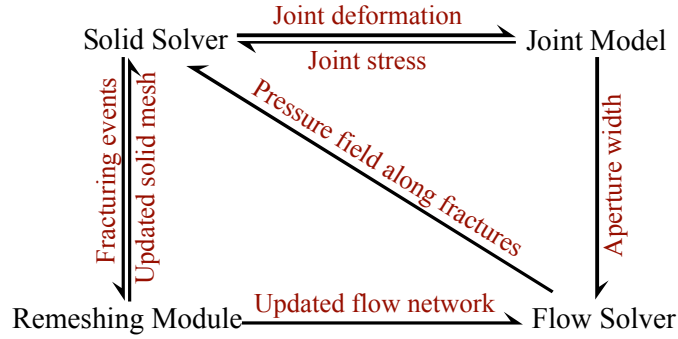


Figure 1 Important modules in the hydraulic fracturing simulator and their coupling.

3. FORMULATION OF INDIVIDUAL MODULES

3.1 FEM solid solver

The finite element module uses the six-node iso-parametric triangular plain-strain element known as the Linear Strain Triangle or the Veubeke triangle, and linear elasticity and small deformations are assumed for the intact material response. The solver uses central-difference explicit time-integration scheme. At each time step, t , the nodal force vector $\mathbf{F}_i(t)$ acting on a node i has four contributions: 1) elastic deformation of the elements connected to the node, 2) fluid pressure if the node is associated with a flow cell, 3) contact stress if this node is associated with a closed joint, and 4) external forces such as those acting at the stress-controlled boundaries. In the explicit time-integration scheme, the dynamic responses are solved on a nodal basis as follows.

$$\ddot{\mathbf{u}}_i(t) = \frac{\mathbf{F}_i(t) - \mathbf{F}_i^C(t)}{m_i} \quad (1)$$

$$\dot{\mathbf{u}}_i(t + \Delta t_s/2) = \dot{\mathbf{u}}_i(t - \Delta t_s/2) + \ddot{\mathbf{u}}_i(t)\Delta t_s \quad (2)$$

$$\mathbf{u}_i(t + \Delta t_s) = \mathbf{u}_i(t) + \dot{\mathbf{u}}_i(t + \Delta t_s/2)\Delta t_s \quad (3)$$

where \mathbf{u}_i , $\dot{\mathbf{u}}_i$, and $\ddot{\mathbf{u}}_i$ are the nodal displacement, velocity, and acceleration vectors, respectively. \mathbf{F}_i^C is the nodal damping force, and only the mass-proportional term of the Rayleigh damping is used in this model. To reduce the computational constraints, the high frequency components in the dynamic response are filtered through the use of the damping term, which is commensurate with the quasi-static assumptions of the process. The mass of an element is distributed to the six nodes, with 1/19 of the element mass assigned to each vertex node and 16/57 to each mid-edge node (Section 16.2.4 in [21]). Δt_s is the time increment used in the solid solver and a Courant-Friedrichs-Lewy (CFL) coefficient of 5% is used to ensure numerical stability.

3.2 Hydrodynamics solver for discrete flow network

Fluid flow in open rock fractures is idealized as laminar flow between two parallel plates employing lubrication theory. The governing equations used in typical hydraulic fracturing models are

$$\frac{\partial q}{\partial l} + \frac{\partial w^h}{\partial t} = 0 \quad (4)$$

$$\kappa \frac{\partial P}{\partial l} = -q \quad (5)$$

$$\kappa = \frac{(w^h)^3}{12\mu_f} \quad (6)$$

where l represents the length along the fracture; q is the local flow rate in the fracture at a given cross-section; w^h is the local time-dependent hydraulic aperture size; P is the local fluid pressure; and κ represents the permeability of the fracture, which is a function of the dynamic viscosity μ_f of the fluid and the local aperture size w^h . Equation (4) is the continuity (mass conservation) equation; equation (6) is the permeability equation, according to the laminar parallel plate flow assumption. These governing equations are solved with a two-dimensional finite volume method (FVM) formulated based on a three-dimensional approach described by Johnson and Morris [22]. This approach and the modifications are described here.

Implementations of FVM employ either node-centered (vertex-centered) or element-centered (cell centered) formulations, and our model uses the latter. To avoid ambiguity, we use the nomenclature of “cell” to denote a finite volume flow element and “element” to denote a solid finite element. As shown in Figure 2, flow connections (corresponding to fracture networks in the solid phase) are discretized and visualized as line segments. For a given cell, i , the parameters correspond to length, L_{Ci} , fluid mass inside the cell, m_{Ci} , volume, V_{Ci} , hydraulic aperture size, w_i^h as well as the associated permeability, κ_{Ci} according to equation (6), fluid pressure, P_{Ci} , etc. where the subscript “ c ” abbreviates “cell”. In a cell representing an open fracture, the aperture size can be approximated by the distance between the two fracture walls calculated in the solid solver and the volume is the product of length (area in 3D) of the cell along the direction of fracture extension and the aperture size, i.e. $V_{Ci} = L_{Ci}w_i^h$. The formulation for closed fractures

subjected to compression will be discussed in Section 3.5. Fluid pressure and aperture size vary within each cell, so P_{Ci} represent the pressure value at the cell center and w_i^h is the average aperture width of the cell.

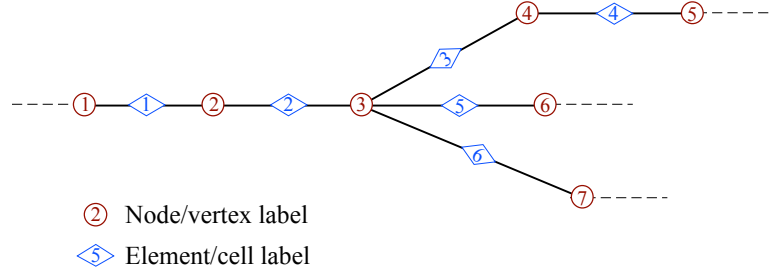


Figure 2 Two-dimensional flow network modeled by the finite volume method.

The follow solver employs an explicit integration scheme, which makes it convenient to couple the flow solver and the solid solver. At each time step, the flow rate of the flow cells is evaluated on a node-by-node basis (note the distinction between the solid node and flow node). Assume there are N_I^C cells connected to the same flow node I ; flow rate from a cell to the common node (i.e. outflow) is assumed to be negative; and the fluid pressure at this node is P_I . The flow rate between cell $I-i$ (the i^{th} cell connected to node I) and node I is

$$q_{I-i} = \frac{2\kappa_{I-i}(P_I - P_{I-i})}{L_{I-i}} \quad (7)$$

To satisfy mass conservation, we have

$$\sum_{i=1}^{N_I^C} q_{I-i} = 0 \quad (8)$$

Combining equations (7) and (8) yields

$$P_I = \frac{\sum P_{I-i} \kappa_{I-i} / L_{I-i}}{\sum \kappa_{I-i} / L_{I-i}} \quad (9)$$

and subsequently the flow rate of each cell can be computed according to equation (7). A special yet very common case is that a flow node is connected to only two cells, denoted as cell i and cell j . In this particular case, the flow rate from cell i to cell j can be simplified as

$$q_{ij} = \frac{2(P_i - P_j)\kappa_{ij}}{L_i + L_j} \quad (10)$$

where κ_{ij} is the homogenized permeability with

$$\kappa_{ij} = \frac{\kappa_i \kappa_j (L_i + L_j)}{\kappa_i L_i + \kappa_j L_j} \quad (11)$$

By looping through all the flow nodes, we calculate the flow rate of each cell from and to its two nodes, thereby obtaining the mass increment and updated fluid mass in the cell. The local fluid pressure is related to the fluid density through the following equation-of-state (EOS)

$$P_{Ci} = \begin{cases} K_f \left(1 - \frac{\rho_{ref} V_{Ci}}{m_{Ci}} \right) & \text{if } m_{Ci} / V_{Ci} \geq \rho_{ref} \\ P_{vap} & \text{if } m_{Ci} / V_{Ci} < \rho_{ref} \end{cases} \quad (12)$$

where K_f is the bulk modulus of the fluid; ρ_{ref} is the reference density of this fluid, namely the density at zero or the datum pressure; P_{vap} is the temperature-dependent vapor pressure of this fluid which is assumed to zero, as the pumping pressure is typically many orders of magnitude higher than the vapor pressure. For any given fluid, the three parameters μ_f , K_f , and ρ_{ref} are dependent on temperature, and to a lesser extent, the pressure. These parameters are assumed to be constant in all the numerical examples of this paper unless otherwise indicated, but temperature- and pressure-dependent material parameters can also be specified in the model. At the end of this step, fluid pressure is calculated for all the flow cells and the procedure is repeated in successive time steps. The coupling between the solid phase deformation and the fluid flow is completed through the joint model, which applies the fluid pressure to the solid mesh elements that are interfaced with the cell and alters the aperture according to the geometric distance of the interfacing surfaces. Despite the simple form, this approach captures salient features of flow in narrow joints due to a pressure gradient, and mass conservation and pressure variation in flow channels with constantly varying volume (i.e. varying aperture size). The second mechanism can cause discontinuity in the system and violate equation (4), which is mediated through the equation-of-state (12).

In this approach, fluid bulk modulus K_f acts as a component of the contact stiffness as well as of the EOS. The governing equations (4) to (6) are essentially formulation for incompressible fluid but a compressibility term K_f is used in the equation-of-state to relate fluid density to pressure. The role of K_f in this solver is similar to that of material density in an explicit solid solver for quasi-static problems. That is, as a pseudo-inertial term, the fluid compressibility can be judiciously reduced to achieve a longer critical time step without sacrificing accuracy of the quasi-static analysis. We have empirically found that as long as the value of K_f is significantly greater than the fluid pressure, the simulation results are insensitive.

3.3 Fracturing criterion

A fracturing criterion determines whether new fracture surface should be generated and along which direction the fracture should propagate by evaluating certain mechanical quantities at tips of existing fractures. The fracturing criterion in the current model is based on the “critical stress intensity factor” concept in linear elastic fracture mechanics (LEFM). Mode-I and mode-II stress intensity factors (SIF), K_I and K_{II} are calculated using the generalized displacement correlation (GDC) method and the propagation direction is determined using a maximum circumferential stress criterion for mixed-mode fracturing. Details of the GDC method and the evaluation of its accuracy are described in a separate paper [23] and we present the essence of this method here for completeness of the current paper.

Generalized displacement correlation method

In the original displacement correlation methods [24-29], SIF's are calculated from nodal displacements near the fracture tip based on analytical solutions for near-tip region displacement. It requires the use of special quarter-point elements [24,27] in the first layer of elements around each tip, which makes it very difficult to be used in simulations of dynamic fracture propagations, where locations of fracture tips constantly evolve and are not known *a priori*. To overcome this problem, we have developed a generalized form of this method, called the generalized displacement correlation (GDC) method, which uses regular linear or quadratic finite element types and can produce accurate results with relatively coarse mesh without near-tip refinement.

The finite element mesh near a fracture tip is shown in Figure 3. Quadratic elements (six-node triangle or eight-node quadrilateral) with mid-edge nodes are used. For plain-strain condition, SIF's can be calculated as

$$K_I = -\frac{\sqrt{\pi} C_I G (2u_{\theta}^A - 2u_{\theta}^{A'} - u_{\theta}^B + u_{\theta}^{B'})}{2(1-\nu)(2-\sqrt{2})\sqrt{l_E}} \quad (13)$$

$$K_{II} = -\frac{\sqrt{\pi} C_{II} G (2u_r^A - 2u_r^{A'} - u_r^B + u_r^{B'})}{2(1-\nu)(2-\sqrt{2})\sqrt{l_E}} \quad (14)$$

where G is the shear modulus of the solid; ν is the Poisson's ratio; l_E is the characteristic length of the element as denoted in Figure 3; C_I and C_{II} are correction multipliers; u_r and u_{θ} are the polar and angular displacements of reference points relative to the fracture tip. The GDC formulation is similar to that of the original displacement correlation method with the main difference being that the two reference points A and A' are mid-edge nodes of regular quadratic elements, instead of special quarter-point nodes. The multipliers C_I and C_{II} are necessary for correcting the errors induced by regular finite elements' inability to characterize the square-root displacement term in the near-tip region. They were found in [23] to be functions of tip-region mesh configuration, element type, mesh size relative to crack length, and Poisson's ratio. Among these factors, the element type is fixed (six-node quadratic triangle) in our model, and the effects of mesh size and Poisson's ratio can be ignored for most geo-engineering purposes. The meshing scheme used in all the examples of the present paper consists of two common tip-region element configurations as shown in Figure 4 and the corresponding correction multipliers are also shown in the figure.

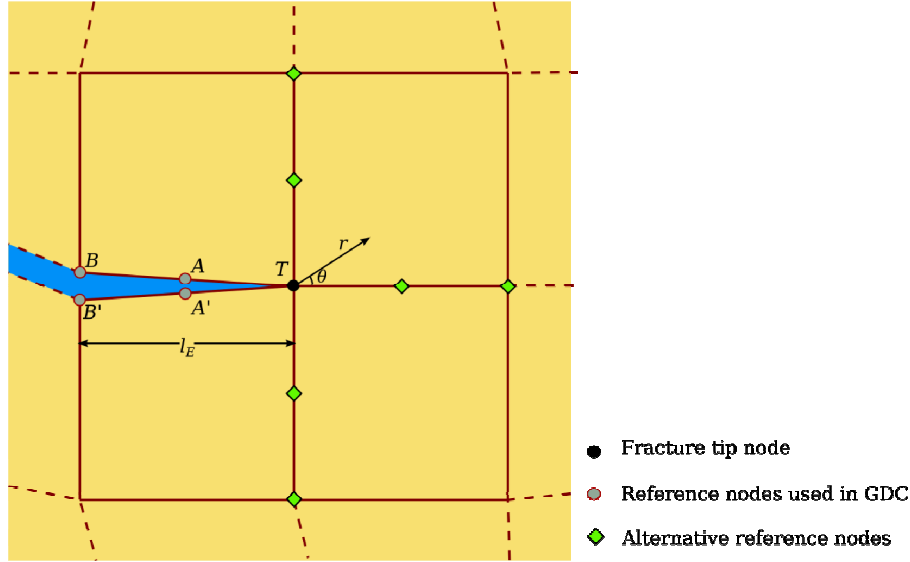


Figure 3 Typical mesh arrangement around a fracture tip. A polar coordinate system is established with its origin at the tip. The reference points used in equations (13) and (14) are denoted as small circles, whereas alternative reference points shown as diamonds can also be used with modified formulations as elaborated in [23].

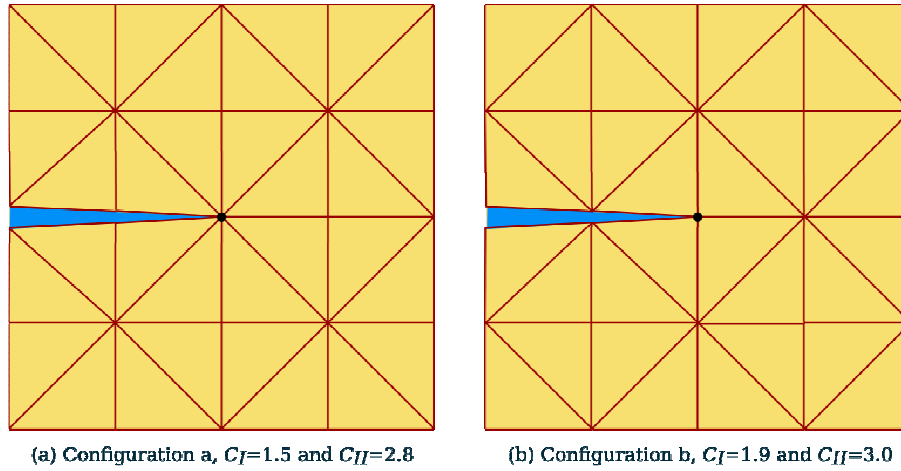


Figure 4 Two common tip-region mesh configurations used in this study and the corresponding GDC correction multipliers.

Fracturing criterion and fracture propagation direction

When the SIF's at a tip are known, the well known fracturing criteria [30, 31] can be directly applied and these criteria usually also predicts fracture propagation directions. In our current implementation of the numerical models, a simplified form of the criteria is adopted based on the constraint that fracture can only follow element boundaries. Although it is theoretically possible to allow a fracture to propagate along an arbitrary direction through element partition or the extended finite element method (XFEM) [16], such methods will make the implementation of the model unacceptably expensive and complex, especially because of the coupling of multiple modules and the large number of possible scenarios of

fracture intersections. The adopted meshing scheme shown in Figure 4 allows a fracture to propagate along seven or three directions (with 45° and 90° increments, respectively) from a tip. However, at a scale larger than the element size, a fracture can propagate along almost any direction by combining many element edges. Nevertheless, the fracturing criterion to be adopted only needs to determine along which candidate edge the fracture should propagate.

The simplified fracture criterion is triggered when $K_I^2 + K_{II}^2 \geq K_{I_crit}^2$ and $K_I > 0$, where K_{I_crit} is the mode-I critical stress intensity factor (i.e., toughness) of the matrix rock. The second condition ($K_I > 0$) dictates that a fracture should not grow unless it is completely open. In the absence of pressurized fluid, all fractures in natural geological formations should be closed and compressive stress is transferred through the contact stress of the two walls of the fractures. As the fracture is pressurized with fluid, the two walls may slide as the normal contact stress, which is essentially the effective normal stress, decreases. Therefore, K_{II} may significantly develop before the fracture is open. However, due to the kinematical constraints posed by the closed fractured, fracture growth is bounded. This bounded sub-fracturing is homogenized in our model by only allowing fractures that are completely open to propagate.

Once the above triggering criteria are met, we calculate the normal stress on all the candidate edges at their mid-edge nodes. The fracture will propagate along the edge with the greatest normal stress (tension is positive). The stress component resembles the circumferential stress used in some classical criteria (e.g. [30]), but it is evaluated at a distance of half the edge length instead of at the tip to be consistent with the approach of separating the entire edge during the time step.

The above empirical criterion was found to yield reasonable results, as demonstrated by the numerical example in Section 6.1, where a hydraulic fracture propagates in a heterogeneous *in situ* stress field.

3.4 Adaptive remeshing algorithm

When the fracturing criterion determines that a fracture should grow along an identified finite element edge, this edge is flagged “fracture-ready” and the adaptive remeshing module is invoked. We use the idealized example shown in Figure 5 to demonstrate how the solid mesh and flow cells are updated.

An edge is considered to be external if there is only one element attached to it, whereas there are always two and only two elements attached to an internal edge. An external edge either represents the free boundary of the rock mass, or one of the walls along a fracture interface. Each time a fracture-ready edge is identified, the two nodes attached to this edge are examined. A given node will be split if either two of the edges connected to this node are fracture-ready or one of the edges connected to this node is fracture-ready while two of the edges are external. Figure 5(a) illustrates this approach with edge 8 and edge 13 flagged as fracture-ready. Subsequently, node 5 is split from the first condition and nodes 4 and 9 are split due to the second condition. Figure 5(b) shows the mesh configuration after the aforementioned remeshing has taken place. Each node that has been split generated two daughter nodes. For instance, nodes 12 and 13 are the daughter nodes of node 5. The daughter nodes belong to the new solid mesh while the mother nodes are detached from the solid mesh and attached to the newly created flow cells

(cell 1 and cell 2). Reusing the nodes and edges that have been detached from the solid mesh ensures that intersecting fractures will result in correct connectivity of the new flow cells. For instance, edge 5 is flagged at a later step, and subsequently, nodes 12 and 2 are split. The new flow cell 3 should not be connected to node 12, which has just been split, but to node 5, the mother node of node 12 as shown in Figure 5(c). During the remeshing process, the mapping between mother nodes and daughter nodes, and that between mother edges and daughter edges is established and stored. Such information is used frequently during the simulation because we apply the fluid pressure from flow cells (which were all previously solid element edges) to their daughter edges as stress boundary conditions to the solid solver. Meanwhile, the locations of the daughter nodes and daughter edges are used to update the locations of the flow cells and the aperture sizes.

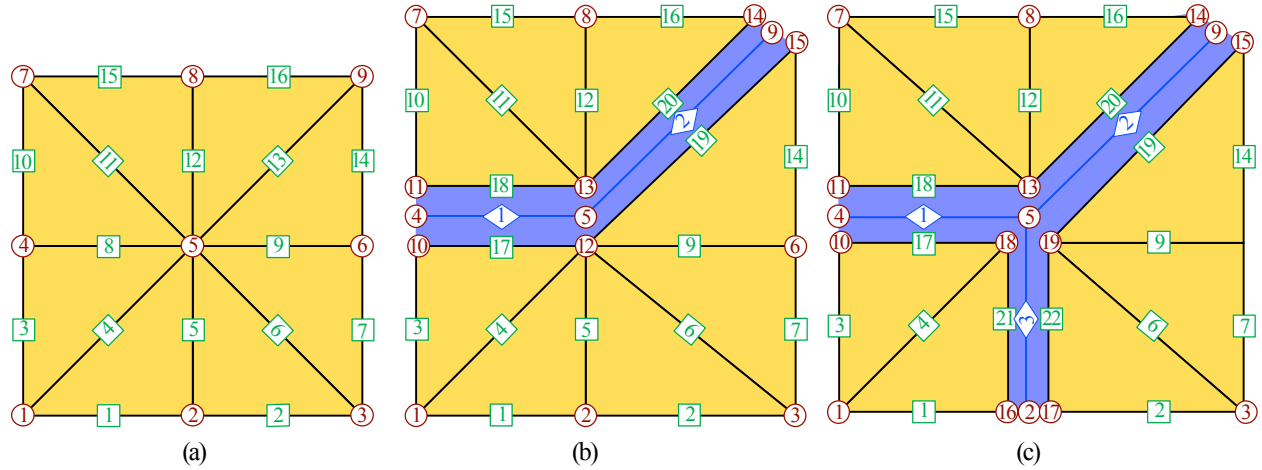


Figure 5 Adaptive remeshing of the finite element model to create new fractures. (a), (b), and (c) represent three states of the same mesh. The labels for edges are placed at mid-edge, and the mid-edge nodes are not shown. Because of the unique correspondence between the edges and the mid-edge nodes, mid-edge nodes are always split when the corresponding edge is split.

3.5 Joint model

Joint behaviors involved in a hydraulic fracturing process, such as dilation associated with shear deformation, reversed and cyclic loading, joint asperity degradation, and their influences on hydraulic conductivity are very complex, and sophisticated constitutive models are often needed to deal with these behaviors (e.g. [32-34]). Here we have implemented a simplified form of the joint model that handles the most basic behaviors including the opening, closing, shear deformation and sliding. As illustrated in Figure 1, the essential function of the joint model in this numerical model is to receive information regarding rock deformation from the solid solver, calculate stress responses and permeability changes, and feed this information to the solid and flow solvers.

Figure 6 shows two solid elements on the opposing sides of a fracture. Two edges, denoted as edge p and edge q , of these elements represent the two opposing walls along the fracture. Edge p is geometrically characterized by its mid-point \mathbf{x}^p in the vector form, its length L^p , a unit outer-pointing normal vector \mathbf{n}^p , and a unit tangential vector \mathbf{t}^p . Similar variables can be defined for edge q and are not repeated here.

These two edges are the daughter edges of the same edge in the original non-fractured solid mesh, so the lengths are the same ($L^p = L^q$) if the small difference in deformation of the two elements in the tangential direction is ignored. The two edges are assumed to be parallel, i.e. $\mathbf{n}^p + \mathbf{n}^q \approx \mathbf{0}$. The normal and tangential components of the distance between the mid-points of the two edges are

$$\delta_n = (\mathbf{x}^q - \mathbf{x}^p) \cdot \mathbf{n}^p \quad (15)$$

$$\delta_t = (\mathbf{x}^q - \mathbf{x}^p) \cdot \mathbf{t}^p \quad (16)$$

The rate of change of the above quantities, $\dot{\delta}_n$ and $\dot{\delta}_t$ can be calculated using similar formulations but with the location vectors replaced with velocity vectors. Because the relative displacement of the two sister edges in the tangential direction in hydraulic fracturing simulations is usually very small compared with the length of the edges, only contacts between sister edges are evaluated. In other words, it is possible that a very small segment of edge p can interact with a segment of the edge next to edge q along the fracture face, but this type of interaction is ignored in the model and no neighbor-sorting is performed to update nearest neighbors, which both limits and expedites the calculation.

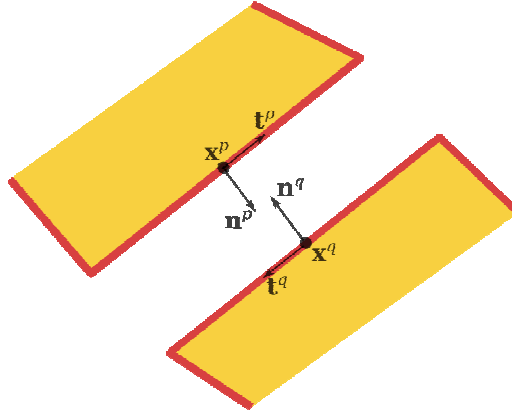


Figure 6 Geometrical characterization of two opposing edges along a fracture. The distances between the two edges are exaggerated for illustration purposes.

When $\delta_n < 0$, the two elements that these two edges attached to penetrate into each other geometrically, representing the state that the two walls along the fracture are in contact where contact stresses should be calculated and returned to the solid solver. The absolute value of δ_n is equivalent to the joint closure as used in rock mechanics. The normal contact stress and the tangential contact stress are calculated using the following equations:

$$(\sigma_n)_{t+\Delta t} = (\sigma_n)_t + k_n \dot{\delta}_n \Delta t \quad (17)$$

$$\tau_{t+\Delta t} = \begin{cases} \tau_t + k_s \dot{\delta}_t \Delta t & \text{if } |\tau_t + k_s \dot{\delta}_t \Delta t| < |(\sigma_n)_{t+\Delta t}| \mu_J \\ \text{sign}(\tau_t) |(\sigma_n)_{t+\Delta t}| \mu_J & \text{otherwise} \end{cases} \quad (18)$$

where k_n and k_s are the normal stiffness and shear stiffness of the joint with a dimension of stress/length. It is well known that both k_n and k_s are highly nonlinear, and they are strongly correlated. The response in

the cases illustrated here are not sensitive to joint stiffness, so these are treated as constants for illustration. μ_f is the coefficient of friction of the walls along the fracture; $\text{sign}()$ is a function returning the sign (positive or negative) of the argument. The Coulomb failure criterion is enforced through equation (18). Note that although the omission of shear dilation is appropriate for the scope of the present paper, this mechanism can play a significant role in other problems. The combination of the contact stress and the fluid pressure should be applied to the edges along the fracture as stress boundary conditions.

When $\delta_n > 0$, we term it the mechanical aperture (also termed the storage aperture in the literature) of the fracture. As mentioned in Section 3.2, it is assumed that the permeability of an open fracture ($\delta_n > 0$) obeys the cubic law expressed in equation (6), i.e. $w^h = \delta_n$. When a fracture is closed ($\delta_n < 0$), it can still conduct fluid flow because of the partly continuous void space between the two walls left by the imperfect matching of the asperities on the opposing sides. Under this condition, the permeability is a function of many factors, including roughness and strength of the joint walls, the mismatch of the two walls, effective compressive normal stress, and shear dilation. These factors are not considered in the examples in this paper, and we instead use the following simplified relationship between the equivalent hydraulic aperture size w^h and δ_n :

$$w^h = \begin{cases} \delta_n & \text{if } \delta_n > w_0^h \\ w_0^h & \text{otherwise} \end{cases} \quad (19)$$

where w_0^h is the “residual” equivalent hydraulic aperture size of a closed fracture, and it is assumed to be a constant regardless of the closure and stress of the joint. Note that the “equivalent” aperture size of a closed fracture is calculated from the permeability of the fracture according to equation (6). It does not represent the physical opening of the two walls in contact, but it conveniently has a dimension of length.

4 MODEL VERIFICATION AGAINST THE KGD MODEL

4.1 The KGD model and its compatibility with the proposed numerical model

The KGD hydraulic fracture model was independently developed by Khristianovic and Zhelton (1955) [5], and Geertsma and de Klerk (1969) [8]. Since it is based on assumptions that are compatible with those of the proposed numerical model in this paper, we use the KGD model as the reference for model verification.

The KGD model concern the propagation of a single fracture driven by fluid pumped into the fracture from the wellbore at a constant flow rate of q_0 , as shown in Figure 7. It assumes plane-strain deformation, linearly elastic, homogeneous and isotropic media, and laminar Newtonian flow obeying the cubic law, which are consistent with the proposed numerical model. The KGD model assumes the flow rate everywhere along the fracture is the same as that at the wellbore when calculating pressure loss. This simplification is not needed in the numerical model and the effects of this assumption are discussed in Section 4.3. The propagation of fracture is controlled by the assumption that there is no gap (vacuum) between the front of the fluid and the fracture tip. Therefore, the KGD model essentially assumes the

fracture propagation is in the fluid viscosity-controlled regime, and the rock toughness is not explicitly considered. The setup of the numerical model can adopt the same assumption as described in Section 4.2, but a more general case with finite rock toughness will be discussed in Section 4.4.

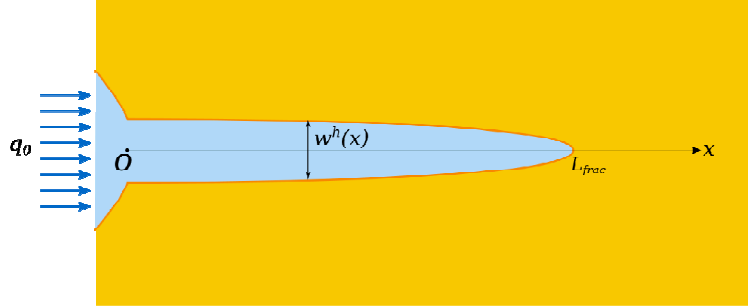


Figure 7 Geometrical characteristics of a KGD fracture. The well is partly shown. The model implies that there is another identical fracture on the other side of the well symmetrical to the one shown.

Pressurized fluid drives the fracture to propagate along the direction perpendicular to the minimum compressive principal stress. Closed-form solutions for various quantities, such as fracture length L_{frac} and aperture width at the wellbore w_0^h at any given time t are available, such as the set derived by Valko and Economides (1995):

$$L_{frac}(t) = 1.078 \left(\frac{E' q_0^3}{\mu_f} \right)^{1/6} t^{2/3} \quad (20)$$

$$w_0^h(t) = 2.36 \left(\frac{\mu_f q_0^3}{E'} \right)^{1/3} t^{1/3} \quad (21)$$

where $E' = 2G/(1-\nu)$ is the plane-strain modulus of elasticity.

4.2 Numerical realization of the KGD model

The simulated domain has dimensions of 100 m and 120 m in the x and y directions, respectively and is discretized into 24,000 elements with a mesh pattern shown in Figure 4. The core mesh is then extended to approximately 1,000 m in each dimension with progressively larger elements to mitigate boundary effects. Slip boundary conditions are applied to the edges. At the left side boundary where the injection well is located this applies a symmetrical condition, consistent with the assumption in the KGD model. Because of the linear elasticity assumptions of the model, the *in situ* stress applied at the boundary will not affect the net pressure results, consistent with the KGD model. Simulation parameters used in this and subsequent analyses (whenever applicable) described in the paper are listed in Table 1.

Table 1 Parameters of the numerical model for the simulation of the KGD model

Parameters	Value
Rock, shear modulus G	8.3 GPa
Rock, Poisson's ratio ν	0.2
Fluid, dynamic viscosity μ_f	0.001 Pa·s
Fluid, bulk modulus K_f	2.2 GPa
Flow rate at wellbore q_0	1.0, 2.0 ^a , and 4.0 liters per second (L/s) per meter thickness of reservoir
Residual hydraulic aperture width w_0^h	0.02 mm

Note: ^a baseline case simulation.

To realize the zero-toughness and no-vacuum assumptions of the KGD model, the critical SIF (K_{I_crit}) in the model is a small finite value (1,000 Pa·m^{1/2}). The fracturing criterion is only checked when the flow cell connected to the tip is fully filled with fluid, i.e. $m_{Ci}/V_{Ci} \geq \rho_{ref}$. When a new flow cell and the associated fracture are created, a fluid lag exists. Meanwhile, the aperture and volume of this cell continue to grow along with permeability. The fracture will start propagating from the current tip when the cell is fully filled and the calculated K_I is greater than the threshold value.

The growth of the fracture length calculated using the numerical model for the three injection rates listed in Table 1 is compared with the corresponding KGD analytical solutions in Figure 8. For the baseline case ($q_0=2.0$ L/s per meter reservoir thickness), three snapshots of aperture width along the fracture at $t=20, 40$, and 80 seconds are shown in Figure 9. The KGD model assumes the cross section of the fracture to have an elliptical shape while the numerical model calculates the aperture width based on deformation in the solid phase and no such assumption is needed. At each moment, the integral of the aperture width along the fracture is the total volume of the fracture, which is the product of the injection flow rate and the injection duration. Compared with the analytical solution, the numerical model predicts a slightly shorter fracture length and slightly wider aperture at the well. Since a number of approximations had to be made in the derivation of the KGD solution which can be relaxed in the numerical model (e.g., constant flow rate along the fracture), the small differences do not necessarily indicate error of the numerical model.

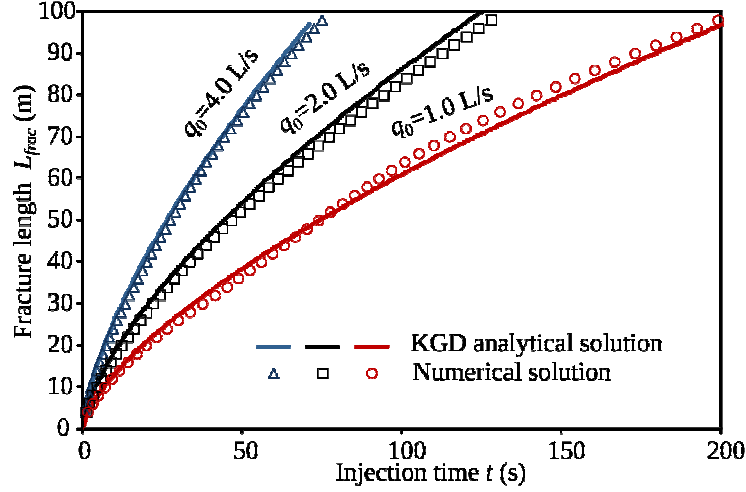


Figure 8 Comparison between the numerical model and the KGD analytical solution in terms of fracture growth rate.

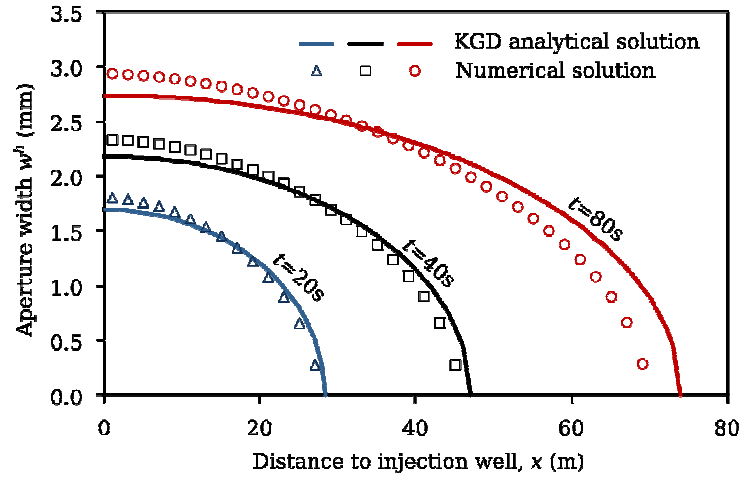


Figure 9 Comparison between the numerical model and the KGD analytical solution in terms of aperture distribution along the fracture.

4.3 Toughness-dominated regime

The propagation of fracture in the original KGD model is dominated by viscous flow of the fluid and a key assumption is that there is no gap (i.e. vacuum) between the front of fluid and the fracture tip. In this section, we derive the formulation for hydraulic fracturing in rock with a high critical stress intensity factor and compare the numerical model with the analytical solution. We assume in this regime aperture of the fracture is wide enough that pressure loss of the fluid along the fracture is negligible compared with the fluid pressure at the tip, so the net pressure is ΔP is a constant in the fracture from the wellbore to the fracture tip. This validity of this assumption in the numerical examples is established later in this section. Two wings of fractures grow simultaneously from the well towards opposite directions and their combination can be modeled as a planar fracture in an infinite medium with its center at the wellbore. Assuming at time t the length of each wing is $L_{frac}(t)$, the volume of fluid in one wing is

$$q_0 t = \frac{\Delta P \pi L_{frac}^2}{E'} \quad (22)$$

where E' is the plane-strain modulus of elasticity defined in Section 4.1, and q_0 is the fluid injection rate into each wing which is a constant for a simulation. The net pressure ΔP is determined by the condition that the mode-I stress intensity factor at the tip equals to the rock toughness K_{I-crit} , namely

$$\Delta P (\pi L_{frac})^{1/2} = K_{I-crit} \quad (23)$$

Plugging equation (22) into (23), we can obtain

$$L_{frac}(t) = \pi^{-1/3} \left(\frac{q_0 E' t}{K_{I-crit}} \right)^{2/3} \quad (24)$$

Under this finite-toughness condition, the length of the fracture is proportional to the injection time raised to the exponent of 2/3, similar to the original KGD model shown in equation (20). However, the viscosity of the fluid does not influence the fracture growth rate, but the rock toughness does. To numerically model this finite-toughness condition, the same numerical model described in Section 4.2 is adopted with the no-vacuum-at-tip restriction removed. Two cases with rock toughness values of 5.0 and 10.0 MPa·m^{1/2} are simulated, and the flow rate q_0 is assumed to be 2.0 liters per second (L/s) per meter thickness of reservoir. As shown in Figure 10, the numerical results match the analytical solution reasonably well.

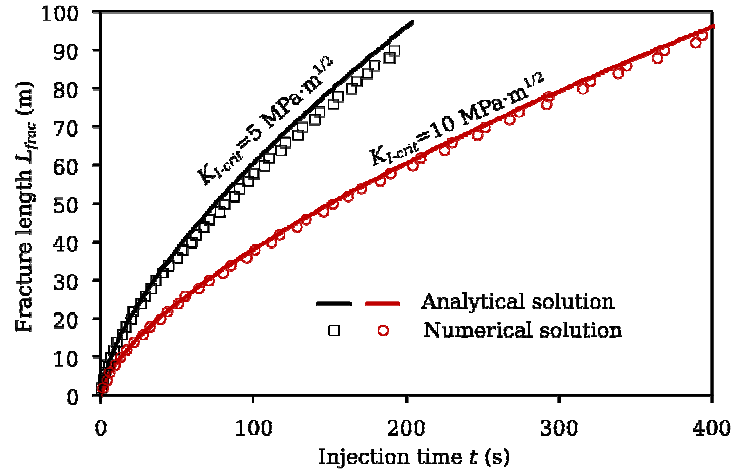


Figure 10 Comparison between the analytical solution and the numerical simulation results for the finite-toughness scenarios.

To check the assumption that the pressure loss along the fracture can be ignored in these cases, we examine the following situation. For the case with $K_{I-crit}=5.0$ MPa·m^{1/2} at $t=75.2$ seconds, the fracture length L_{frac} is approximately 50 meters. The mean aperture size is 3.0 mm ($\bar{w}^h = q_0 t / L_{frac}$). For a constant flow rate of $q_0=2.0$ L/s per meter reservoir thickness through a fracture with a uniform aperture width of 3.0 mm, the pressure drop is 44 kPa according to equations (5) and (6), which is approximately 11% of the net pressure required to create a stress intensity factor of 5.0 MPa·m^{1/2} at the fracture tip. For the case with $K_{I-crit}=10.0$ MPa·m^{1/2} at a crack length of 50 meters, this ratio is 0.7%. Therefore, omission

of pressure loss along the fracture for the rock toughness-dominated scenarios is reasonable for the parameters tested. Note that the critical SIF values used in these two examples are higher than those of typical rocks, in order to ensure that the fracture propagation is in the toughness-dominated regime. Real hydraulic fracture propagation should be somewhere between these viscosity-dominated and toughness-dominated bounds. Though this is naturally accommodated by the proposed numerical model, analytical solutions for these intermediate scenarios are not available.

5 MODEL VALIDATION AGAINST LABORATORY TESTS

5.1 Description of the laboratory test

In the previous section, we have verified that the numerical model can appropriately handle the coupling between the fluid phase and the solid phase during the propagation of a single fracture. We further validate the model in this section in terms of its ability to simulate the interaction between a propagating fracture that intersects an existing fracture.

Blanton [36] fabricated synthetic rock blocks using “hydrostone” with an existing fracture embedded at variable angles with respect to the specimen, as illustrated by the horizontal cross-section in Figure 11. Each rock block was then placed in a triaxial cell for testing. The vertical compressive stress (out-of-plane in Figure 11; compression is positive) is 20 MPa, and the two horizontal principal stress components $\sigma_h < \sigma_H \leq 20$ MPa. Water was injected into a hole at the center of each specimen to create a hydraulic fracture propagating in the plane normal to the minor principal stress σ_h and subsequently intersecting the existing fracture at an angle of approach θ_{apr} . The variables investigated in Blanton’s study included the magnitudes of σ_H and σ_h and the angle of approach θ_{apr} . Testing parameters and the observed interaction modes between the hydraulic fracture and the existing fracture for selected cases are listed in Table 2.

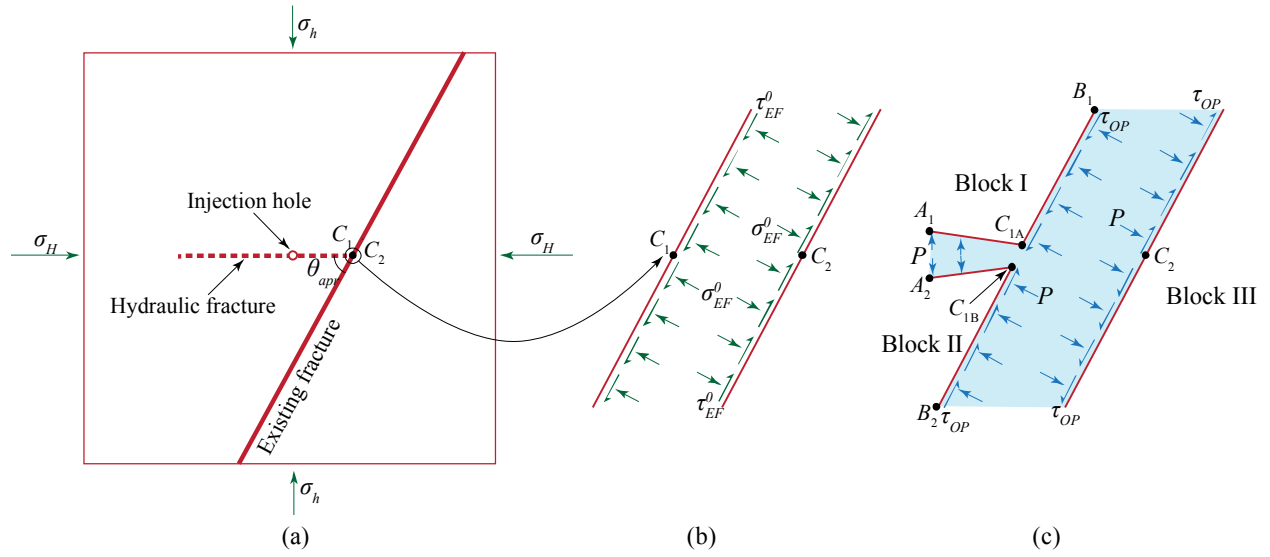


Figure 11 Schematic views of Blanton (1982)'s laboratory tests [36] on the interaction between a hydraulic fracture and an existing fracture. The two horizontal dimensions of each specimen are 30 cm x 30 cm. (a) Triaxial stress applied to the specimen and the geometrical configuration of the two fractures; (b) stress along the existing fracture before the hydraulic fracture intersects it, and (c) *additional* stress along the existing fracture induced by the opening of the hydraulic fracture and the interaction between the two fractures.

5.2 Mechanisms for different interaction modes

Three modes of interaction including “crossing”, “arrest”, and “opening” were reported in Blanton’s study. The mechanisms behind these three modes have been extensively studied using a variety of methods (e.g. [37–40]) in the literature. We briefly review the process of a hydraulic fracture intersecting an existing fracture to help the determination of the key parameters of the numerical model and the interpretation of the simulation results.

Before the stress field in the specimen is significantly altered by the creation and propagation of the hydraulic fracture, the normal and shear stress (σ_{EF}^0 and τ_{EF}^0 , respectively; the subscript “ EF ” stands for “Existing Fracture” and the superscript “ 0 ” indicates that this is the initial condition) as shown in Figure 11(b) are functions of σ_H , σ_h , and θ_{apr} and are listed in Table 2. When the hydraulic fracture has intersected the existing fracture at point C_1 but has not break the other wall of the fracture at C_2 , additional stresses will act on the existing fracture: First, pressurized fluid will start to flow into the existing fracture. If we assume the fluid pressure at a given moment and location along the existing fracture is $P(t)$ and the effective normal stress (i.e. contact normal stress between the two walls along the fracture) at the same time and location is $\sigma_{EF}(t)$, the following relationship holds

$$\sigma_{EF}(t) + P(t) \approx \sigma_{EF}^0$$

This is approximate because the stress field might be perturbed near the intersection. The effective normal stress along the existing fracture decreases as the fluid pressure in it increases. Since solid block *I* (enclosed by A_1 - C_{1A} - B_1) and block *II* (A_2 - C_{1B} - B_2) tend to move away from each other, especially when fluid pressure P is significantly higher than σ_h , this motion will create additional shear stress τ_{OP} along the fracture as shown in Figure Figure 11(c). Note that the subscript “ $_{OP}$ ” stands for “opening”. This shear stress increment has opposite directions at the two sides of point C_2 , and is the primary driving mechanism of the stress intensity factor at C_2 .

Table 2 Different scenarios tested in Blanton (1982) [36], observed interaction modes, and numerical simulation results.

Case ID ^a	θ_{apr}	Principal stress (MPa)		Interaction mode	Stress on ex. frac. before pumping		$\frac{\tau_{EF}^0}{\sigma_{EF}^0 - \sigma_h}$	Max. SIF at C_2 (MPa·m ^{1/2})
		σ_H	σ_h		σ_{EF}^0	τ_{EF}^0		
CT-20	90°	14.0	5.0	crossing	14.0	0.0	0.00	0.69
CT-21	60°	14.0	5.0	arrest	11.7	3.9	0.58	0.36
CT-8	60°	20.0	5.0	crossing	16.2	6.5	0.58	0.59
CT-4	60°	12.0	10.0	opening	11.5	0.9	0.58	0.13
CT-22	45°	10.0	5.0	opening	7.5	2.5	1.00	Negligible
CT-14	45°	14.0	5.0	arrest	9.5	4.5	1.00	Negligible
CT-13	45°	16.0	5.0	arrest	10.5	5.5	1.00	Negligible
CT-12	45°	18.0	5.0	arrest	11.5	6.5	1.00	Negligible
CT-11	45°	20.0	5.0	arrest	12.5	7.5	1.00	Negligible

Note: ^a Case ID here is the “Test #” in Blanton’s original paper.

The role of hydraulic pressure in this process is twofold. In order to generate an SIF that is great enough to break the fracture wall at point C_2 and allow the hydraulic fracture to cross the existing fracture, high fluid pressure is needed to create additional shear stress τ_{OP} along the existing fracture by pushing blocks *I* and *II* apart. However, a higher fluid pressure will reduce the effective normal stress on the existing fracture and the two blocks might be able to slide along the wall, preventing the creations of a high SIF. The relative significance of these mechanisms depends on the existing normal and shear stresses on the fracture before fluid flow into the existing fracture. Next we consider an idealized scenario. Assume when the hydraulic fracture breaks one of the fracture walls at point C_1 and intersects the existing fracture, the fluid pressure $P = \sigma_h$. Note that $P \geq \sigma_h$ is the necessary condition (but no sufficient condition) for the hydraulic fracture to propagate. Because the hydraulic pressure merely balances σ_h , blocks *I* and *II* do not have a significant tendency to move apart from the fracture and therefore $\tau_{OP} \approx 0$. If we assume no sliding takes place along the existing fracture under this condition, the mobilized coefficient of friction is $\tau_{EF}^0 / (\sigma_{EF}^0 - P) = \tau_{EF}^0 / (\sigma_{EF}^0 - \sigma_h) = \tan(90^\circ - \theta_{apr})$ with the derivation process omitted here and the value of

mobilized coefficient of friction for all the scenarios listed in Table 2. Under this condition, configurations with smaller approaching angles have a stronger tendency to slide along the existing fracture at the moment the hydraulic fracture intersects the existing fracture. If the fluid pressure near the intersection point increases beyond σ_h , then the sliding tendency is enhanced, because 1) the effective normal stress is further reduced, and 2) the shear stress is increased as least on one side of point C_2 .

5.3 Numerical simulation results

The nine scenarios in Table 2 are simulated using the numerical model. The original paper [36] did not provide information on the fluid pressure for each specimen. The actual pressure should be dependent on a number of factors, including the minor principal stress σ_h , dynamic response of the pumping system, and the compliance of the hydraulic system. A clue that helps estimate the pressure at the injection hole is the difference between the “opening” mode and the “arrest” mode. Opening means that the hydraulic fracture is first arrested by the existing fracture and the pumping pressure is higher than normal stress ($\sim \sigma_{EF}^0$) induced by the boundary condition. We found that a fluid pressure of $\sigma_h + 3.0$ MPa is consistent with the observations in the laboratory testing results and this pressure is used as the flow boundary condition in the simulations. The toughness (i.e. critical stress intensity factor) of the hydrostone is unknown. To quantify the effects of the external variables on the ability or potential of the hydraulic fracture to cross the existing fracture, we use a small toughness value ($10 \text{ kPa} \cdot \text{m}^{1/2}$) on the left-hand-side of the existing fracture, so that the hydraulic fracture can propagate towards the existing fracture. We do not allow the mesh to fracture to the right of the existing fracture in the simulation. Instead, we track the mode-I stress intensity factor K_I at point C_2 and the maximum value achieved by each specimen is presented in Table 2. Other numerical simulation parameters are presented in Table 3.

Table 3 Parameters of the numerical model for the simulation of the Blanton experiments

Parameters	Value
Rock, shear modulus G	8.3 GPa
Rock, Poisson's ratio ν	0.2
Fluid, dynamic viscosity μ_f	0.001 Pa·s
Fluid, bulk modulus K_f	2.2 GPa
Fluid pressure at the injection hole	$\sigma_h + 3.0$ MPa
Joint, residual hydraulic aperture width w_0^h	0.005 mm
Joint, coefficient of friction μ_J	0.7
Joint, normal stiffness k_n	500 GPa/m
Joint, shear stiffness k_s	1.0 GPa/m
Average element dimension	~ 1 cm

Figure 12 shows the evolution of K_I at point C_2 and the fluid pressure near C_2 for two cases, CT-8 and CT-21, with their only difference being σ_H . After the fracture wall at C_1 breaks, K_I at C_1 increases as the pressure increases, due to the associated increase of τ_{OP} . K_I suddenly drops when the pressure is high

enough to allow sliding to occur along the existing fracture. The case with a higher σ_H value has a stronger resistance to sliding than the other case, and therefore K_I is able to continue to grow to a higher peak value before the fluid pressure is high enough to induce sliding. As mentioned in Section 5.3 and shown in Table 2, for the specimens with $\theta_{apr}=45^\circ$, the mobilized coefficient of friction at C_2 needs to be higher than 1.0 to sustain significant τ_{OP} but the coefficient of friction used in the simulation is 0.7. Therefore, K_I values significantly higher than zero cannot develop in those cases.

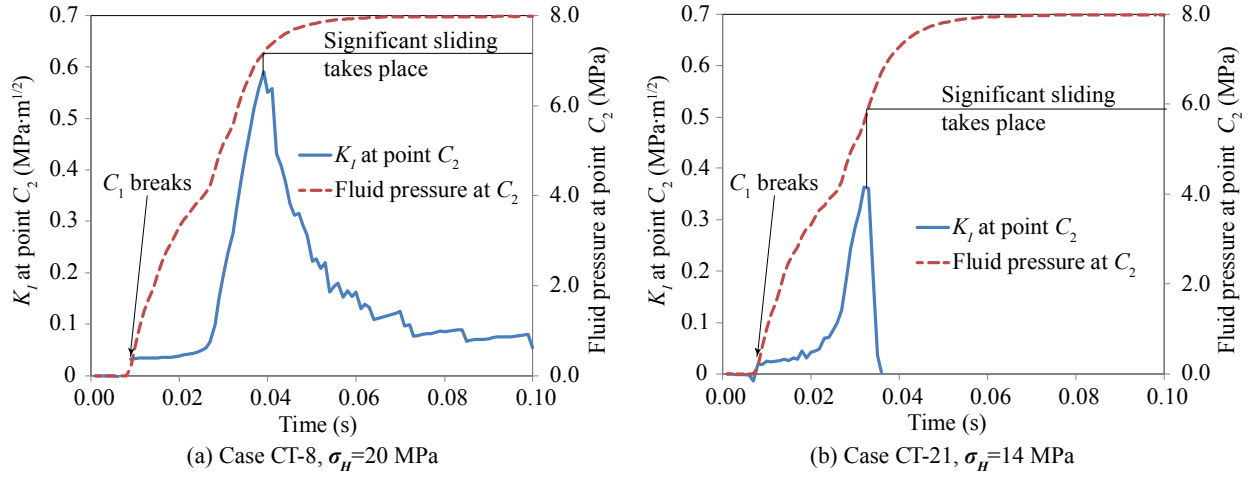


Figure 12 The evolution of K_I at point C_2 and fluid pressure near C_2 for two cases.

Based on the simulation results, we find that if the toughness of the hydrostone is greater than 0.36 but smaller than 0.59 $\text{MPa}\cdot\text{m}^{1/2}$, the numerical model can exactly reproduce the observed phenomena in Blanton's laboratory tests. Although the toughness of this particular material used cannot be precisely determined, the study in this section demonstrates that the proposed explicit coupling simulation strategy and the numerical model can adequately reflect the physical mechanisms governing the interaction between two intersecting fractures. A significant advantage of this method compared with other methods used for this problem is that the temporal evolution of the states of each phase can be explicitly resolved and the effects of each variable in this physical process can be studied independently.

6. DEMONSTRATION OF SIMULATION CAPABILITY

6.1 Fracture propagation in heterogeneous field

The proposed numerical model only allows fracture to initiate and propagate along interfaces between neighboring solid elements, namely edges in the mesh, which raises mesh dependency concerns. In this section, we examine this effect through a numerical example where a hydraulic fracture propagates in a solid medium with a heterogeneous field.

The boundary conditions applied to a $200\text{ m} \times 100\text{ m}$ solid medium are shown in Figure 13(a). Slip boundaries are applied at the left and bottom boundaries. The stress applied at the other two boundaries is

denoted in the figure and the resultant nodal stress tensors are visualized as ellipses. The major principal stress is horizontal at the left side of the medium and it gradually becomes vertical at the right side. Fluid is pumped into the domain through a perforation shown in the figure. Since hydraulic fracture tends to grow in the direction perpendicular to the minor principal stress, it is expected that it will first propagate horizontally and then gradually turn vertical.

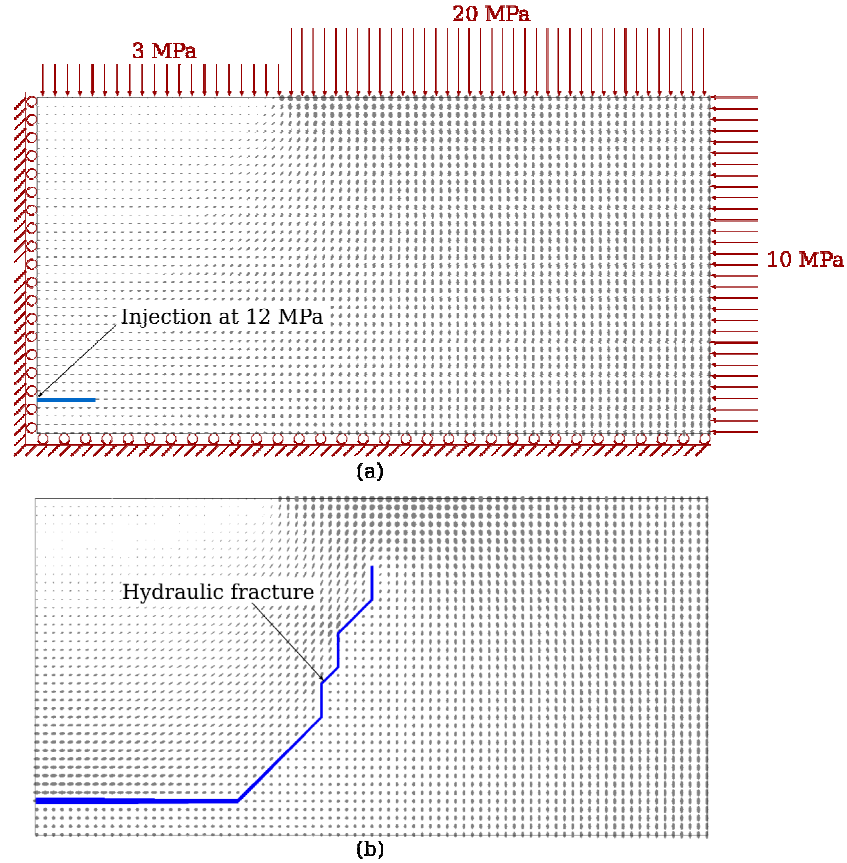


Figure 13 Hydraulic fracture propagation in a medium with a heterogeneous stress distribution. (a) The boundary conditions and stress tensor distribution before hydraulic fracturing. (b) The path of the hydraulic fracture and the stress tensor at the end of the simulation. The 2D stress tensor at each node is represented by an ellipse. The lengths of the two axes of an ellipse are proportional to the two principal stress components at this point and the orientations of the two ellipse axes coincide with the orientations of the two principal stress components.

The simulation uses parameters similar to those used in Section 4, and the fracture path obtained and the stress tensor distribution at the end of the simulation are shown in Figure 13(b). Although the simulated hydraulic fracture abruptly switches trajectory by 45°, due to the mesh constraints, the model is able to capture the overall propagation path of the fracture which is dictated by the applied boundary conditions. Therefore, the mesh dependency of fracture path appears to be not a serious issue at a scale that is significantly larger than the element size. The fracturing criterion is “smart” enough to find the optimum combination of element edges to form a continuous fracture path that is consistent with the mechanical conditions applied in the model.

6.2 Study of responses of a reservoir with isotropically oriented natural fractures

In this section we use the proposed numerical model to investigate the stimulation of a virtual reservoir with the presence of largely isolated natural fractures with uniformly distributed orientations. The variables to be studied include the orientation of the far-field principal stress axes and the degree of stress anisotropy. The reservoir setting is hypothetical and the primary objective of these simulations is to study whether the numerical simulation results can reasonably respond to the variation of external variables.

Natural fractures and meshing strategy

The simulation domain interior to the boundary mesh is 100 m long in both dimensions (from 0 to 100 m in the x /horizontal direction and from -50 m to 50 m in the y /vertical direction), and the triangle elements have edges approximately 1 m long. The mesh is based on the meshing scheme shown in Figure 3 but a small and random perturbation is imposed on the location each node to introduce some randomness to the mesh as shown in Figure 14(c). Progressively larger element sizes are employed to extend the simulation domain to 1,000 m in each dimension, and the far-field stress conditions are applied at the boundary of the extended mesh. A preexisting natural fracture system is randomly generated and mapped onto the edges of solid elements within the core simulation domain as shown in Figure 14 (a). The fractures are largely isolated with lengths ranging from 6 m to 18 m with a mean of 11 m. The orientations of these fractures are uniformly distributed between 0 and 180 degrees rotating from the x direction. The injection well for hydraulic stimulation is placed at $x=0$ and $y=0$. At the bottom, top, and right boundaries of the core simulation domain, a zero-pressure boundary condition is specified in the flow solver as shown in Figure 14 (b), so these three boundaries are treated as fluid “sinks”. Simulation parameters used in this suite of examples are similar to those used in Sections 4 and 5 and are thus not repeated here.

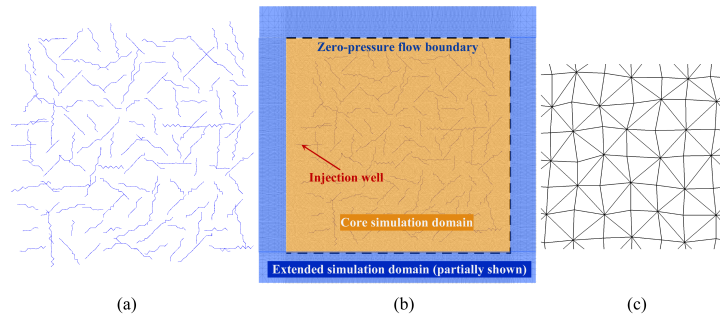


Figure 14 Preexisting natural fractures and the meshing strategy. (a) The randomly generated natural fractures; (b) the core simulation domain and the extended domain; and (c) perturbed mesh to introduce randomness to the fracture path.

The effects of principal stress orientation

Three simulations are performed in the study of the effects of principal stress orientation. In the baseline case (A-1), the far-field stress is $\sigma_{xx}=15$ MPa, $\sigma_{yy}=10$ MPa, and $\sigma_{xy}=0$ (compressive stress is positive in this example). Fluid is pumped into the system through the injection well denoted in Figure 14(b) at a constant pressure of 14 MPa. The simulation result of the stimulated fracture system for the baseline case at the end of the stimulation are shown in Figure 15(a), where the fractures (including both natural and created fractures) that are engaged (i.e. connected to the injection well and pressurized by the fluid) in the stimulation are shown in red color and the unaffected fractures are in gray. Note that the aperture widths are magnified by twenty times to enable clear visualization. The distribution of stress component σ_{yy} at the end of the stimulation is shown in Figure 15(b) where the additional compressive stress created by the pressurized fractures along the horizontal direction and the tensile stress at fracture tips in the pumping front are visible. The simulation results for the two additions cases, A-2 and A-3, where the principal stresses have rotated counterclockwise and clockwise, respectively, by 30 degrees are shown in Figure 15(c) and (d).

It is well known that hydraulic fractures tend to propagate along the plane of the least compressive (far-field) stress in homogeneous media. In all the three cases, the general orientations of the engaged fracture systems are consistent with the predicted directions based on the far-field principal stress orientation. The heterogeneity in the rock body due to the presence of natural fractures inevitably affects the paths along which hydraulic fractures propagate, making them deviate from the ideally predicted paths. These effects appear to be local, with a minimal influence on the general trends of the fractures. Moreover, these effects, embodied by the interactions between fractures are well reflected in the numerical model. This study also confirms the observations made in Section 6.1 regarding the minimal mesh dependency of fracture paths in the proposed numerical method. In the current meshing scheme, the inter-element interfaces, namely potential fracture paths are generally along directions 0° , 45° , 90° , and 135° from the x -axis with some randomness introduced by the mesh perturbation. However, this does not prevent the fractures from propagating along directions $\pm 30^\circ$.

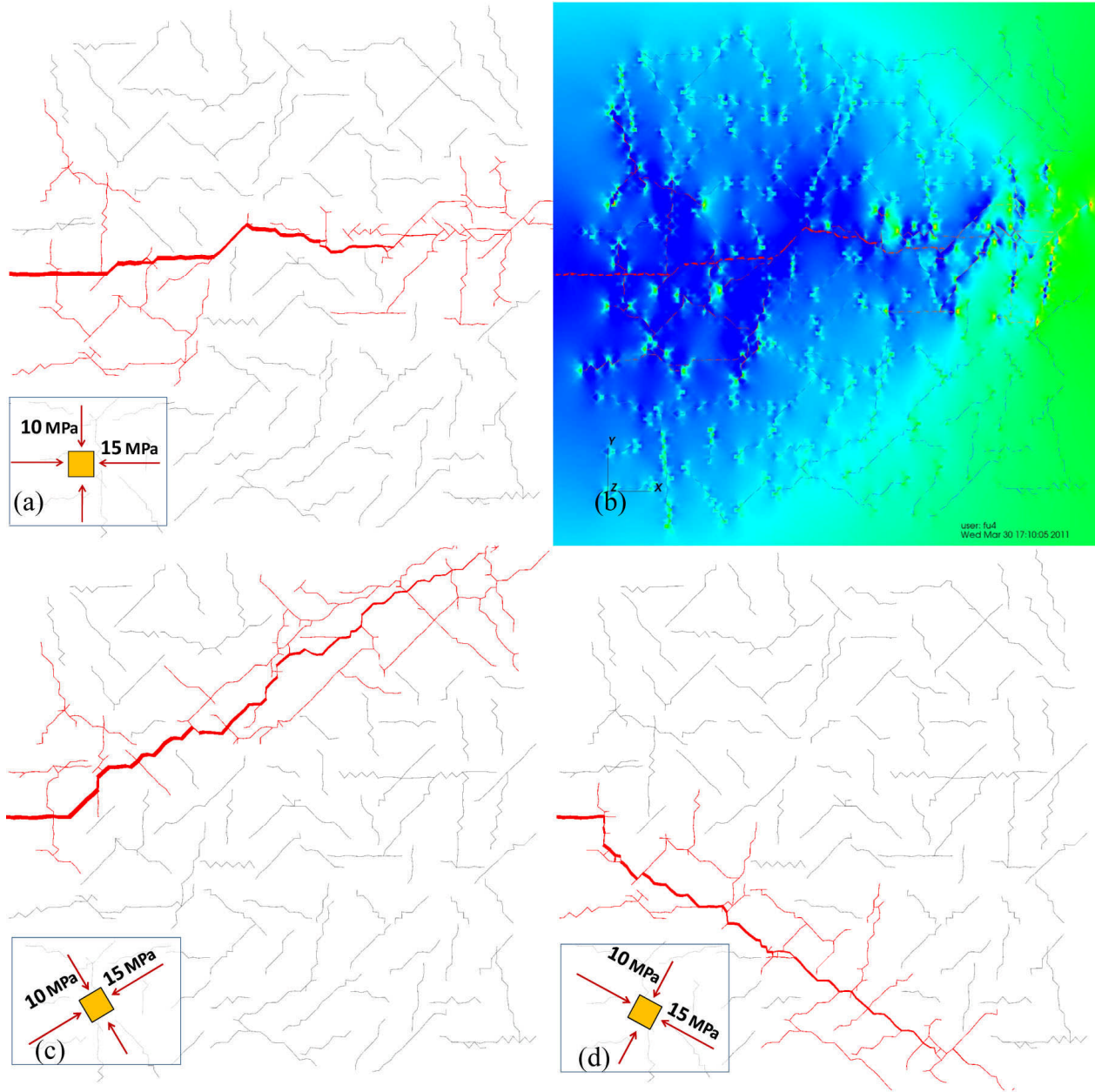


Figure 15 Stimulated fracture networks with different far-field principal stress orientations. Preexisting natural fractures and newly created fractures that are engaged by the stimulation are shown in red color, whereas unaffected natural fractures are in gray. The orientations of the principal stresses are schematically shown in each figure. (a) Baseline case A-1 where the major principal stress aligns with the x -axis; (b) distribution of σ_{yy} in case A-1 at the end of stimulation, with the blue end of the color spectrum indicating stress that is more compressive and the red end being more tensile or less compressive; (c) case A-2, the principal stress axes have rotated counterclockwise by 30 degrees from the baseline; and (d) case A-3, the principal stress axes have rotated clockwise by 30 degrees from the baseline.

The effects of stress anisotropy

In this study, the baseline case B-1 is the same as the baseline case A-1 in the previous study. The additional scenarios have the same far-field stress in the y -direction ($\sigma_{yy} = 10$ MPa) as the baseline case but smaller compressive stresses $\sigma_{xx} = 12$ and 10 MPa for cases B-2 and B-3, respectively. Note that the far-field stress for case B-3 is isotropic. The pumping pressure for all the cases remains 14 MPa. The simulation results are shown in Figure 16 in a fashion similar to that of Figure 15, with fractures engaged in the stimulation highlighted. The result for B-1 is the same as that for A-1, and is thus not repeated in Figure 16.

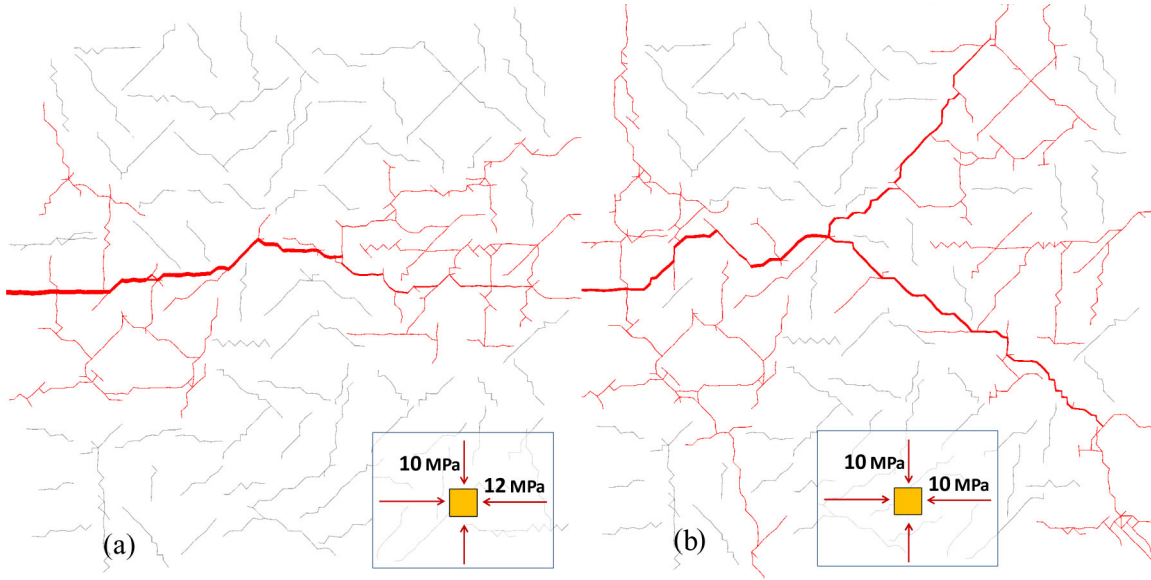


Figure 16 Stimulated fracture networks under different degrees of stress anisotropy but the same principal stress axis orientation. The far-field stress state is denoted in each figure. Note that the baseline case is shown in Figure 15(a).

The stimulated fracture network for case B-2 is similar to that of the baseline case, with a slightly more diffuse pattern of fracture growth at the far side from the injection well, presumably because the reduced compressive stress in the x -direction provides more flexibility in the choice of viable propagation paths by the hydraulic fracture. In case B-3, there is no preferential fracture propagation direction since the far-field stress is isotropic. Four major branches of fractures have developed as the results of the stimulation along largely random directions, but these four branches tend to propagate away from each other. This is because if two parallel fractures are close to each other, the compressive stress in the rock matrix induced by the fluid pressure tends to impede the development of tensile zones at the fracture tips, retarding further propagation.

7 CONCLUDING REMARKS

In this paper we present an explicit coupling simulation strategy for hydraulic fracturing in complex natural fracture systems. In the proposed method, each of the physical processes involved in hydraulic fracturing is modeled by a separate module of the simulator and the interactions between these processes are embodied by the data/information sharing between these modules. Since multiple processes of rather

different natures are involved and they influence each other in many different ways, this explicit strategy provides a flexible simulation framework for complex hydraulic fracturing phenomena. Because the operations of these modules are sufficiently decoupled in this explicit coupling methodology, upgrading an individual module with more realistic (and inevitably more complex) models can be done without significantly affecting other modules. Therefore, although only the baseline simulation capability using relatively simple models is described in this paper, the presented simulation framework will remain unchanged if more complex problems are to be simulated.

The verification and validation of the numerical model focus on relatively simple but well-quantifiable phenomena in rock-fracture-fluid systems. Quantitative data, at either the laboratory or field scale are not available for the interaction between hydraulic fractures and existing natural fracture networks. However, since the interactions between fractures in a complex fracture network can be decomposed into the propagation of individual fractures and the interactions within individual pairs of fractures, the verification and validation in this paper provide a reasonable physical and mechanics base, on which the credibility of the proposed model is built.

The numerical model using this explicit coupling strategy is known to be computationally expensive. The main reason is that the physical phenomena being simulated are not only complex, but also ill-conditioned. The simulation domain is often hundreds of meters in each direction whereas typical aperture width is a small fraction of a millimeter. A deformation that is considered small “noise” in the solid solver may induce dramatic (by orders of magnitudes) oscillation of fluid pressure in the flow solver. Since the model has to essentially resolve multiple dynamic physical processes with characteristic length-scales across several orders of magnitude, the time steps used in both the solid and flow solvers are necessarily very small. As an example, each of the simulations in Section 6.2 costs hundreds of CPU-hours on currently mainstream computers. A number of modeling and computational technologies, including more efficient solvers, more intelligent time-stepping, hybrid solvers, and massively parallelized processing are currently being developed and implemented to enable this model to be used more effectively.

Acknowledgments

The authors gratefully acknowledge the Geothermal Technologies Program of the US Department of Energy for support of this work under the Enhanced Geothermal Systems Program. Additional support was provided by the LLNL LDRD project “Creating Optimal Fracture Networks” (#11-SI-006). The authors also would like to acknowledge their collaborators at the Lawrence Livermore National Laboratory. This work was performed under the auspices of the U.S. Department of Energy by Lawrence Livermore National Laboratory under Contract DE-AC52-07NA27344. This manuscript was approved to be released by LLNL with a release number LLNL-JRNL-519272.

References

1. Warpinski NR, Teufel LW. Influence of geologic discontinuities on hydraulic fracture propagation. *Journal of Petroleum Technology* 1987; 39(2): 209-220, DOI:10.2118/13224-PA.
2. Nolte KG, Smith MB. Interpretation of fracturing pressures. *Journal of Petroleum Technology*. 1981;33(9):1767–1775, DOI: 10.2118/8297-PA.
3. Warpinski NR, Branagan PT, Peterson RE, Wolhart SL, Uhl JE. Mapping hydraulic fracture growth and geometry using microseismic events detected by a wireline retrievable accelerometer array. *Proceedings of SPE Gas Technology Symposium 1998*; Society of Petroleum Engineers, DOI: 10.2118/40014-MS.
4. Cipolla CL, Wright CA. Diagnostic techniques to understand hydraulic fracturing: what, why, and how. *Proceedings of SPE/CERI Gas Technology Symposium 2000*; Society of Petroleum Engineers, DOI: 10.2118/59735-MS.
5. Khristianovic SA, Zheltov YP. Formation of vertical fractures by means of highly viscous liquid. In *Proceedings of the Fourth World Petroleum Congress 1955, Rome*, 579–586.
6. Hubbert KM, Willis DG. Mechanics of hydraulic fracturing. *Transactions of The American Institute of Mining and Metallurgical Engineers* 1957; 210(6):153-163.
7. Perkins TK, Kern LR. Widths of hydraulic fractures. *Journal of Petroleum Technology* 1961; 13: 937-949.
8. Geertsma J, de Klerk F. A rapid method of predicting width and extent of hydraulically induced fractures. *Journal of Petroleum Technology* 1969; 21: 1571-1581.
9. Nordgren RP. Propagation of a vertical hydraulic fracture. *Society of Petroleum Engineers Journal* 1972; 12: 306-314.
10. Adachi J, Siebrits E, Peirce A, Desroches J. Computer simulation of hydraulic fractures. *International Journal of Rock Mechanics and Mining Sciences* 2007; 44: 739-757, DOI: 10.1016/j.ijrmms.2006.11.006.
11. King GE, Haile L, Shuss J, Dobkins TA. Increasing fracture path complexity and controlling downward fracture growth in the Barnett shale. *Proceedings of SPE Shale Gas Production Conference, 2008*, (SPE 119896); DOI: 10.2118/119896-MS.
12. Detournay E. Propagation regimes of fluid-driven fractures in impermeable rocks. *International Journal of Geomechanics* 2004; 4(1):35-45, DOI: 10.1061/(ASCE)1532-3641(2004)4:1(35).
13. Garagash DI, Detournay E. Plane-strain propagation of a fluid-driven fracture: Small toughness solution. *Journal of Applied Mechanics* 2005; 72(6): 916-928, DOI: 10.1115/1.2047596.
14. Siebrits E, Peirce AP. An efficient multi-layer planar 3D fracture growth algorithm using a fixed mesh approach. *International Journal for Numerical Methods in Engineering* 2002; 53(3): 691-717, DOI: 10.1002/nme.308.

15. Galindo Torres SA, Muñoz Castaño JD. Simulation of the hydraulic fracture process in two dimensions using a discrete element method. *Physical Review E* 2007; 75(6):1-9, DOI: 10.1103/PhysRevE.75.066109.
16. Dahi-Taleghani A. Analysis of Hydraulic Fracture Propagation in Fractured Reservoirs : An Improved Model for the Interaction Between Induced and Natural Fractures. Doctoral dissertation, Texas A&M University, 2009.
17. Chen Z, Bungera AP, Zhang X, Jeffrey RG. Cohesive zone finite element-based modeling of hydraulic fractures. *Acta Mechanica Solida Sinica* 2009; 22(5): 443-452, DOI: 10.1016/S0894-9166(09)60295-0.
18. Sarris E, Papanastasiou P. The influence of the cohesive process zone in hydraulic fracturing modelling. *International Journal of Fracture* 2010; 167(1): 33-45. DOI: 10.1007/s10704-010-9515-4.
19. Damjanac B, Gil I, Pierce M, et al. A new approach to hydraulic fracturing modeling in naturally fractured reservoirs. *Proceedings of the 44th US Rock Mechanics Symposium and 5th US-Canada Rock Mechanics Symposium*, Salt Lake City, Utah; 2010, ARMA 10-400.
20. Zhang Z, Ghassemi A. Simulation of hydraulic fracture propagation near a natural fracture using virtual multidimensional internal bonds. *International Journal for Numerical and Analytical Methods in Geomechanics* 2011; 35(4):480-495, DOI: 10.1002/nag.905.
21. Zienkiewicz OC, Taylor RL, Zhu JZ. *Finite Element Method – Its Basis and Fundamentals*. Elsevier Butterworth-Heinemann, 2005, Oxford.
22. Johnson SM, Morris JP. Modeling hydraulic fracturing for carbon sequestration applications. *Proceedings of the 43rd US Rock Mechanics Symposium and the 4th US-Canada Rock Mechanics Symposium*, 2009, Asheville, NC, ARMA 09-30.
23. Fu P, Johnson SM, Settgest RR, Carrigan CR. Generalized displacement correlation method for estimating stress intensity factors. *Engineering Fracture Mechanics*, submitted.
24. Barsoum RS. On the use of isoparametric finite elements in linear fracture mechanics. *International Journal for Numerical Methods in Engineering* 1976; 10(1): 25–37.
25. Shih CF, deLorenzi H, German MD. Crack extension modeling with singular quadratic isoparametric elements. *International Journal of Fracture* 1976; 12(3): 647-651.
26. Tracey DM. Discussion of ‘on the use of isoparametric finite elements in linear fracture mechanics’ by R. S. Barsoum. *International Journal for Numerical Methods in Engineering* 1977; 11(2): 401-402.
27. Barsoum RS. Triangular quarter-point elements as elastic and perfectly-plastic crack tip elements. *International Journal for Numerical Methods in Engineering* 1977; 11(1): 85-98.
28. Ingraffea AR, Manu C. Stress-intensity factor computation in three dimensions with quarter-point elements. *International Journal for Numerical Methods in Engineering* 1980; 15(10): 1427-1445.

29. Banks-Sills L, Sherman D. Comparison of methods for calculating stress intensity factors with quarter-point elements. *International Journal of Fracture* 1986; 32(2): 127-140.
30. Erdogan F, Sih GC. On the crack extension in plates under plane loading and transverse shear. *Journal of Basic Engineering* 1962; 85(4): 519-527, doi:10.1115/1.3656897.
31. Sih GC. Strain-energy-density factor applied to mixed mode crack problems. *International Journal of Fracture* 1974; 10(3): 305-321, DOI: 10.1007/BF00035493.
32. Barton N, Bandis S, Bakhtar K. Strength, deformation and conductivity coupling of rock joints. *International Journal of Rock Mechanics and Mining Sciences & Geomechanics Abstracts* 1985; 22(3): 121-140, DOI: 10.1016/0148-9062(85)93227-9.
33. Cook NGW. Natural joints in rock: Mechanical, hydraulic and seismic behaviour and properties under normal stress. *International Journal of Rock Mechanics and Mining Sciences & Geomechanics Abstracts* 1992; 29(3):198-223, DOI:10.1016/0148-9062(92)93656-5.
34. Yeo IW, de Freitas MH, Zimmerman RW. Effect of shear displacement on the aperture and permeability of a rock fracture. *International Journal of Rock Mechanics and Mining Sciences* 1998; 35(8): 1051-1070, DOI:10.1016/S0148-9062(98)00165-X.
35. Valko P, Economides MJ. *Hydraulic Fracture Mechanics*, Wiley: New York, 1995.
36. Blanton TL. An experimental study of interaction between hydraulically induced and pre-existing fractures. *Proceedings of SPE Unconventional Gas Recovery Symposium*. Pittsburgh, Pennsylvania. Society of Petroleum Engineers; 1982: 559-571, DOI: 10.2118/10847-MS.
37. Renshaw CE, Pollard DD. An experimentally verified criterion for propagation across unbounded frictional interfaces in brittle, linear elastic materials. *International Journal of Rock Mechanics and Mining Science & Geomechanics Abstracts* 1995; 32(3): 237-249, DOI: 10.1016/0148-9062(94)00037-4.
38. Zhang X, Jeffrey RG. Reinitiation or termination of fluid-driven fractures at frictional bedding interfaces. *Journal of Geophysical Research* 2008;113(B8):1-16, DOI: 10.1029/2007JB005327.
39. Akulich AC, Zvyagin AV. Interaction between hydraulic and natural fractures. *Fluid Dynamics* 2008; 43(3):428-435, DOI: 10.1134/S0015462808030101.
40. Gu H, Weng X. Criterion for fractures crossing frictional interfaces at non-orthogonal angles. *Proceedings of the 44th US Rock Mechanics Symposium and 5th U.S.-Canada Rock Mechanics Symposium*. Salt Lake City, Utah; 2010: ARMA 10-198.